

## Asymmetric distribution of Fe-peak elements in Cassiopeia A revealed by XRISM

TOSHIKI SATO ,<sup>1</sup> SHIN-ICHIRO FUJIMOTO ,<sup>2</sup> KOJI MORI ,<sup>3</sup> JUN KURASHIMA,<sup>3</sup> HIROSHI NAKAJIMA ,<sup>4</sup>

PAUL P. PLUCINSKY ,<sup>5</sup> MANAN AGARWAL ,<sup>6</sup> LIYI GU ,<sup>7</sup> ADAM FOSTER ,<sup>5</sup> KAI MATSUNAGA ,<sup>8</sup>

HIROYUKI UCHIDA ,<sup>8</sup> AYA BAMBÀ ,<sup>9,10,11</sup> JACCO VINK ,<sup>6,7</sup> YUKIKATSU TERADA ,<sup>12,13</sup> HIRONORI MATSUMOTO,<sup>14</sup>

LIA CORRALES ,<sup>15</sup> HIROSHI MURAKAMI ,<sup>16</sup> SATORU KATSUDA ,<sup>12</sup> MAKOTO SAWADA ,<sup>17</sup> HARUTO SONODA ,<sup>9,13</sup>

EHUD BEHAR ,<sup>18</sup> MASAHIRO ICHIHASHI ,<sup>9</sup> AND HIROYA YAMAGUCHI ,<sup>13</sup>

<sup>1</sup>Department of Physics, School of Science and Technology, Meiji University, Kanagawa, 214-8571, Japan

<sup>2</sup>National Institute of Technology Kumamoto College, 2659-2 Suya, Koshi, Kumamoto 861-1102, Japan

<sup>3</sup>Faculty of Engineering, University of Miyazaki, Miyazaki 889-2192, Japan

<sup>4</sup>College of Science and Engineering, Kanto Gakuin University, Kanagawa 236-8501, Japan

<sup>5</sup>Center for Astrophysics, Harvard-Smithsonian, MA 02138, USA

<sup>6</sup>Anton Pannekoek Institute/GRAPPA, University of Amsterdam, Science Park 904, 1098 XH Amsterdam, The Netherlands

<sup>7</sup>SRON Netherlands Institute for Space Research, Niels Bohrweg 4, 2333 CA Leiden, The Netherlands

<sup>8</sup>Department of Physics, Kyoto University, Kyoto 606-8502, Japan

<sup>9</sup>Department of Physics, Graduate School of Science, The University of Tokyo, 7-3-1 Hongo, Bunkyo-ku, Tokyo 113-0033, Japan

<sup>10</sup>Research Center for the Early Universe, School of Science, The University of Tokyo, 7-3-1 Hongo, Bunkyo-ku, Tokyo 113-0033, Japan

<sup>11</sup>Trans-Scale Quantum Science Institute, The University of Tokyo, Tokyo 113-0033, Japan

<sup>12</sup>Graduate School of Science and Engineering, Saitama University, 255 Shimo-Ohkubo, Sakura, Saitama 338-8570, Japan

<sup>13</sup>ISAS/JAXA, 3-1-1 Yoshinodai, Chuo-ku, Sagamihara, Kanagawa 252-5210, Japan

<sup>14</sup>Department of Earth and Space Science, Osaka University, Osaka 560-0043, Japan

<sup>15</sup>Department of Astronomy, University of Michigan, MI 48109, USA

<sup>16</sup>Department of Data Science, Tohoku Gakuin University, Miyagi 984-8588, Japan

<sup>17</sup>Department of Physics, Rikkyo University, Tokyo 171-8501, Japan

<sup>18</sup>Department of Physics, Technion, Technion City, Haifa 3200003, Israel

## ABSTRACT

The elemental abundances of the Fe-peak elements (such as Cr, Mn, Fe and Ni) and Ti are important for understanding the environment of explosive nuclear burning for the core-collapse supernovae (CC SNe). In particular, the supernova remnant Cassiopeia A, which is well known for its asymmetric structure, contains three “Fe-rich blobs,” and the composition of the Fe-peak elements within these structures could be related to the asymmetry of the supernova explosion. We report a highly asymmetric distribution of the Fe-peak elements in Cassiopeia A as revealed by XRISM observations. We found that the southeastern Fe-rich region has a significant Mn emission above the  $4\sigma$  confidence level, while the northwestern Fe-rich region has no clear signature. In addition to the significant difference in Mn abundance across these regions, our observations show that the Ti/Fe, Mn/Cr, and Ni/Fe ratios vary from region to region. The observed asymmetric distribution of Fe-peak elements could be produced by (1) the mixing of materials from different burning layers of the supernova, (2) the asymmetric distribution of the electron fraction in the progenitor star and/or (3) the local dependence of the neutrino irradiation in the supernova innermost region. Future spatially resolved spectroscopy of Cassiopeia A using X-ray microcalorimeters will enable more detailed measurements of the distribution and composition of these elements, providing a unique tool for testing asymmetric supernova physics.

**Keywords:** X-ray astronomy (1810) — Supernova remnants (1667) — Nucleosynthesis (1131) — Core-collapse supernovae (304)

## 1. INTRODUCTION

Core-collapse supernova (CCSN) explosion mechanisms remain one of the great unsolved problems in as-

trophysics, with asymmetric dynamics thought to play a central role in driving the explosion (e.g., Janka 2012; Burrows & Vartanyan 2021). The  $\sim$ 340-year-old rem-

nant Cassiopeia A (Cas A) provides an ideal laboratory for studying these asymmetries (e.g., Hughes et al. 2000; Fesen et al. 2006; Grefenstette et al. 2014; Milisavljevic & Fesen 2015; Sato et al. 2021; Milisavljevic et al. 2024; Orlando et al. 2025), exhibiting three prominent Fe-rich plumes that reveal the inhomogeneous nature of the ejecta (e.g., Wongwathanarat et al. 2017).

The mass ratios among Fe-peak elements are known to be key observables that characterize the silicon-burning process ( $\alpha$ -rich freezeout) occurring in the innermost regions of core-collapse supernova explosions. In particular, during  $\alpha$ -rich freezeout the resulting elemental composition is governed by the electron fraction,  $Y_e$ , the peak density, the peak temperature, the rates of temperature and density evolution, and the freezeout timescale (e.g., Woosley et al. 1973; Thielemann et al. 1996). Measurements of these mass ratios can therefore be used to infer the neutron excess and entropy at the explosion center (e.g., Jerkstrand et al. 2015; Sato et al. 2021). Moreover, recent multidimensional supernova simulations predict asymmetric distributions of  $Y_e$  and entropy within the ejecta (e.g., Wanajo et al. 2018; Vartanyan et al. 2018; Fujimoto & Nagakura 2021; Burrows et al. 2024), making Cas A an ideal target for testing these predicted asymmetries.

Several measurements of Fe-peak elements have been carried out in Cas A, including, for example, studies of Mn and Cr. In Sato et al. (2020), the Mn/Cr ratio was used to estimate the progenitor's initial metallicity. Here, the elements processed by the CNO cycle during stellar evolution pile up into  $^{14}\text{N}$ , which is burnt to  $^{22}\text{Ne}$  in the He burning stage through the reactions  $^{14}\text{N}(\alpha, \gamma)^{18}\text{F}(\beta^+)^{18}\text{O}(\alpha, \gamma)^{22}\text{Ne}$ . The  $\beta^+$  decay in this process increases the neutron excess (Timmes et al. 2003). Such neutronization affected by the initial metallicity also occurs in the stellar evolution of massive stars (e.g., Thielemann & Arnett 1985). Thus, the ratio of the neutron-rich element Mn to Cr serves as an indicator of the progenitor's initial metallicity (see also Badenes et al. 2008; Park et al. 2013). Based on the X-ray measurement of these elements, the authors have suggested that Cas A's progenitor formed in a sub-solar-metallicity environment. However, convective mixing within the progenitor can produce an asymmetric  $Y_e$  distribution (e.g., Bazan & Arnett 1994), and contamination from the complete Si-burning region near the explosion center could complicate these interpretations. Therefore, the spatial variation of the Mn/Cr ratio offers important observational insights.

The synthesized yield of Mn is also linked to neutrino irradiation near the explosion center, and Sato et al. (2023) have discussed this possibility within Cas A's Fe-

rich ejecta. Neutrinos can excite heavy nuclei, which subsequently emit nucleons and light nuclei, significantly altering the final composition. This process is called the “ $\nu$ -process” (e.g., Woosley & Haxton 1988; Woosley et al. 1990; Woosley & Weaver 1995; Heger et al. 2005; Yoshida et al. 2005, 2008; Hayakawa et al. 2013, 2018; Sieverding et al. 2018, 2019). In the  $\nu$ -process, neutrino spallation, working on the  $^{56}\text{Ni}$  produced by complete and incomplete Si burning, enhances the Mn abundance through the reaction  $^{56}\text{Ni}(\nu, \nu' p)^{55}\text{Co}$ , where  $^{55}\text{Co}$  decays to  $^{55}\text{Fe}$  and then to stable  $^{55}\text{Mn}$ . Especially in the complete Si burning regime, the production of Mn without the  $\nu$ -process is much smaller than with it (as we show below, and see also Yoshida et al. 2008). In addition to the  $\nu$ -process, the strongly neutrino-processed proton-rich environment can also enhance the Mn abundance at the complete Si burning region (Wanajo et al. 2018), where  $^{55}\text{Mn}$  is initially produced as the proton-rich isotope  $^{55}\text{Ni}$ , which then decays via Co and Fe to  $^{55}\text{Mn}$ . In this case, the innermost material is strongly irradiated by neutrinos during the accretion phase, producing a proton-rich environment that synthesizes  $^{55}\text{Ni}$  effectively. After the accretion phase and the SN shock passage, neutrinos still irradiate the central materials during the cooling phase, so the  $^{56}\text{Ni}(\nu, \nu' p)^{55}\text{Co}$  reaction increases the amount of Mn further. Thus, both the  $\nu$ -process and a proton-rich environment (i.e., the  $\nu p$ -process) can enhance Mn production, which means that we can test the existence of the neutrino interaction by measuring the Mn abundance in the innermost ejecta.

Not only Mn and Cr, but also Ti and Ni, which are also synthesized at the explosion center, have attracted attention as tracers of entropy and neutron excess. Sato et al. (2021) have detected Ti in the Fe-rich structure in Cas A's southeast region and, based on its abundance, showed that this feature represents a high-entropy ejecta plume produced by the neutrino-heating mechanism. Although Ni has similarly been identified, accurately quantifying its synthesized mass has been challenging with previous detectors (see Sato et al. 2021). With the high-resolution X-ray spectroscopy of XRISM's Resolve microcalorimeter (Tashiro et al. 2025; Ishisaki et al. 2025), we can now measure these elements from Ti through Ni with unprecedented precision and probe their spatial variations. In this paper, we investigate the asymmetric distribution of Fe-peak elements in Cas A based on early XRISM satellite observations.

## 2. OBSERVATION AND DATA REDUCTION

We performed a two-pointing observation of Cas A during the XRISM commissioning phase. From these

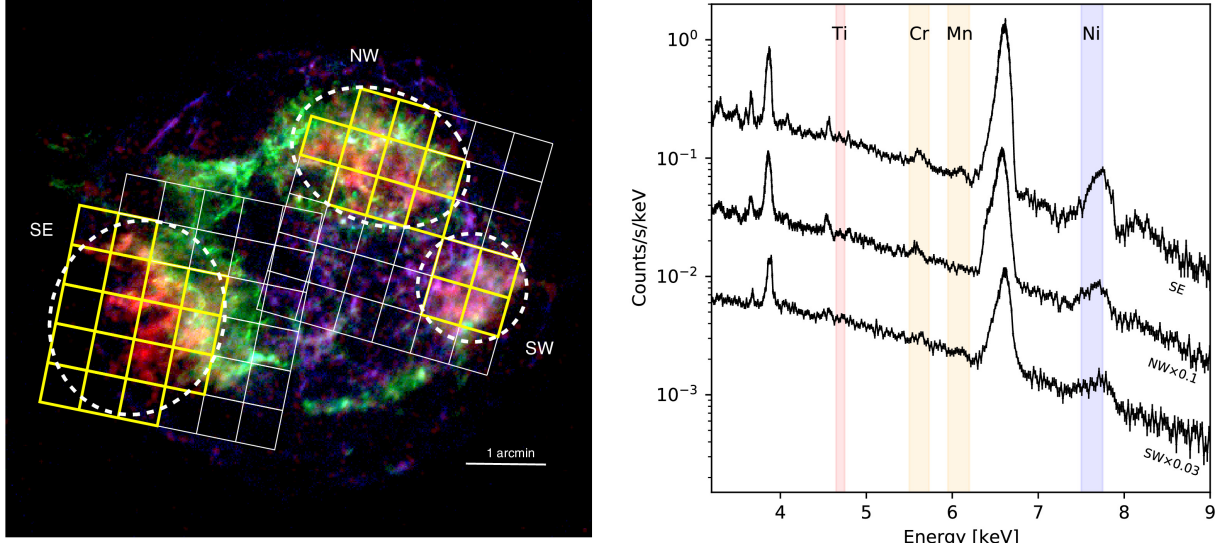


**Figure 1.** *Left:* The field of view of the XRISM/Resolve pointings shown on the three-color image of Cas A taken by Chandra. Red, green, and blue include emission within energy bands of 6.54–6.92 keV (Fe He $\alpha$ ), 1.76–1.94 keV (Si He $\alpha$ ), and 4.2–6.0 keV (continuum), respectively. The dashed ellipses indicate the approximate locations of the three Fe-rich blobs in Cas A.

We extracted the spectra from the pixel regions highlighted in yellow. *Right:* The X-ray spectra observed with XRISM/Resolve, extracted from the regions defined in the left panel. Energy bands corresponding to the He $\alpha$  emissions of Ti, Cr, Mn, and Ni are highlighted in color.

observations, we have already reported on the impact of atomic data and spectral models on derived abundances (Plucinsky et al. 2025), as well as on the measurement of the remnant’s expansion (Bamba et al. 2025; Suzuki et al. 2025; Vink et al. 2025) and the odd-Z elements (Xrism Collaboration et al. 2025) enabled by the Resolve’s high-energy resolution. While Plucinsky et al. (2025) also reported spatial variations in the abundance ratios of the Fe-peak elements, in this paper we present a more detailed analysis and interpretation, with a particular focus on the abundance ratios in the Fe-rich structures. The Resolve fields of view (FoVs) are shown in Fig. 1 (left). Data reduction utilized calibration files from the HEASARC Calibration Database (CALDB). Cleaned event lists were produced with HEASARC software v6.34, applying standard screening during post-pipeline processing, resulting in clean exposure times of 181.3 and 165.7 ks for SE and NW, respectively. For spectral analysis, we selected only the highest-resolution (“Hp”) primary events. The redistribution matrix file (RMF) was generated in “extra-large” mode via `rslmkrmf`, and the ancillary response file (ARF) was generated with `xaarfgen`, adopting Cas A’s surface brightness profile as measured from a 2.0–8.0 keV Chandra X-ray image.

We defined the three Fe-rich regions observed in Cas A (southeast: SW, northwest: NW and southwest: SW) as pixel regions in XRISM/Resolve and extracted the spectrum from each (Fig. 1, right). The high-energy

resolution spectra obtained with Resolve clearly show that the intensity ratios of Cr, Mn, and Ni emission lines vary between regions. In particular, Mn and Ni lines are enhanced in the SE region and suppressed in the NW region, indicating an asymmetric distribution of Fe-peak elements. To verify that these line-ratio variations correspond to true abundance differences, we derived elemental abundances via spectral fitting. Each fit was performed with SPEX v3.08.01 (Kaastra et al. 1996) and XSPEC v12.14.1 (AtomDB v3.1.3) (Arnaud 1996), using the maximum-likelihood  $C$ -statistic (Cash 1979) over the 1.6–12.0 keV band. To account for the non-X-ray background (NXB), we applied the temporal NXB spectral model provided by the XRISM calibration team, constructed from 785 ks of stacked night-Earth observations. This model comprises a power law plus 17 Gaussian components for Al K $\alpha_1$ /K $\alpha_2$ , Au M $\alpha_1$ , Cr K $\alpha_1$ /K $\alpha_2$ , Mn K $\alpha_1$ /K $\alpha_2$ , Fe K $\alpha_1$ /K $\alpha_2$ , Ni K $\alpha_1$ /K $\alpha_2$ , Cu K $\alpha_1$ /K $\alpha_2$ , and Au L $\alpha_1$ /L $\alpha_2$ , L $\beta_1$ /L $\beta_2$ . We note that the level of the NXB is more than order of magnitude below the source spectrum in the energy ranges we are interested in. Thus, our results are insensitive to any uncertainty in the NXB model.

We also investigated the jet structure outside the field of view of Resolve by analyzing the data obtained by XRISM/Xtend (Mori et al. 2024) (Figure 2). As with Resolve, we applied the standard screening, which resulted in a clean exposure time of 215.2 ks for the SE pointing, and generated the RMF file using `xtdrmf` and

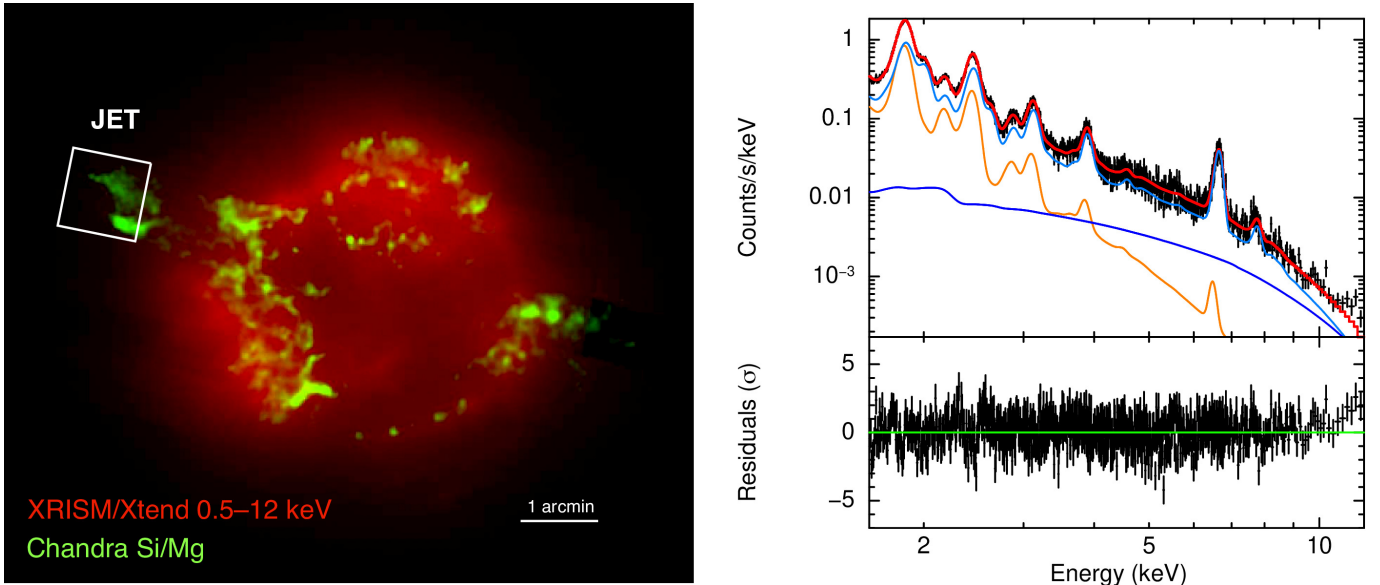


**Figure 2.** *Left:* Two-color image of Cas A obtained with XRISM/Xtend and Chandra. Red indicates the 0.5–12 keV emission observed with Xtend, and green shows the Si-to-Mg line emission ratio map. The spectra were extracted from the white-box region labeled “JET.” *Right:* X-ray spectrum from the JET region (black points) along with the best-fit model (red solid line) in the 1.6–12 keV energy range. The lower panel displays the residuals between the data and the model. The orange, light blue, and blue solid lines correspond to the low-temperature plasma component, the high-temperature plasma component, and the power-law component, respectively.

the ARF file using `xaarfgen`. We generated the background spectrum of the analysis region using the NXB database, and subtracted it from the source region spectrum. In the NW pointing, a charge injection (CI) row intersects the center of the jet structure, which makes the evaluation difficult. Therefore, for Xtend, we analyze only the SE pointing.

### 3. ASYMMETRIC DISTRIBUTION OF FE-PEAK ELEMENTS

We present here a detailed evaluation of the X-ray spectra and the corresponding observational results. Figure 3 presents the results of plasma modeling of the Resolve’s X-ray spectrum in the SE region, and the best-fit parameters are summarized in Table 1. Based on previous observations (Hwang & Laming 2012), we fitted the spectra with a two-temperature non-equilibrium ionization (NEI) model, absorbed by the interstellar medium (ISM) with solar abundances (Lodders et al. 2009). The high-temperature ejecta component was modeled with a plane-parallel shock (`bvvps Shock` in Xspec and `neij` with ‘mode=3’ in SPEX) plasma. Here, the fitting model in Xspec is `phabs*(bvvnei+bvvps Shock+pow)` and that in SPEX is `abs*(neij(mode=1)+neij(mode=3)+pow)`. We allowed the volume emission measure ( $= n_e n_p V_{\text{NEI}}$ , where  $n_e$ ,  $n_p$ , and  $V_{\text{NEI}}$  are the electron density, proton density, and plasma volume, respectively), the electron temper-

ature,  $kT_e$ , and the ionization timescale,  $n_e t$ , line broadening and redshift parameters to vary. Abundances of Mg, Al, Si, P, S, Cl, Ar, K, Ca, Ti, Cr, Mn, Fe, and Ni were left free and tied between both NEI components, while all other elements were fixed at solar values. As shown in Figure 3, when the spectra are fitted with two plasma components at different temperatures, nearly all of the emission from the Fe-group elements that are the focus of this study originates from the high-temperature component. Therefore, even if the abundances are not tied between the two NEI components, our results remain unchanged. The absorption column density,  $N_{\text{H}}$ , was fixed at  $1.9 \times 10^{22}$ ,  $2.0 \times 10^{22}$ , and  $1.5 \times 10^{22} \text{ cm}^{-2}$  for the SE, NW, and SW regions, respectively, with reference to the previous observational result (Hwang & Laming 2012). Even if  $N_{\text{H}}$  is treated as a free parameter, our conclusions remain unchanged (Table 2). In the case where  $N_{\text{H}}$  is allowed to vary freely, the best-fit values of  $N_{\text{H}}$  in the SE, NW, and SW regions are estimated to be  $N_{\text{H}} = (7.3 \pm 0.8) \times 10^{21}$ ,  $(3.7^{+0.7}_{-1.0}) \times 10^{21}$ , and  $(1.6^{+0.1}_{-0.2}) \times 10^{22} \text{ cm}^{-2}$ , respectively, where the results differ significantly from previous studies in all regions except the SW region. During the XRISM/Resolve observations, the gate valve was closed, and photons below  $\sim 1.5$  keV were scarcely detected.

Based on the detailed spectral analysis, we found that the elemental composition ratios vary within the Fe-rich structures of Cas A. The clearest difference appears be-

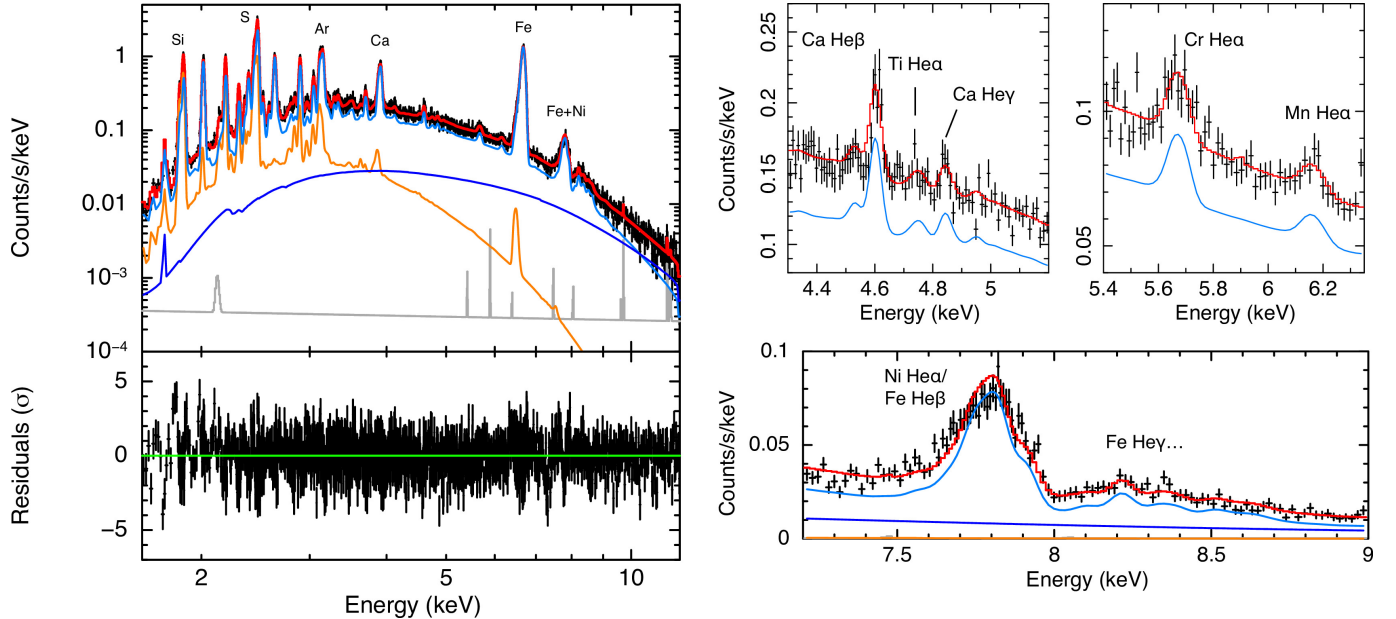


**Figure 3.** X-ray spectrum of the SE region obtained with Resolve (black points) together with the best-fit model (red solid line). The left panel presents the fit in the 1.6–12 keV energy range, while the lower panel shows the residuals between the data and the model. The orange, light blue, blue, and gray solid lines represent the low-temperature plasma model, the high-temperature plasma model, the power-law model, and the NXB model, respectively. The multiple panels on the right show zoomed-in views of the energy bands of Ti, Cr, Mn, and Ni.

tween the SE region and the NW region, and the variation in Mn abundance is especially noteworthy (Table 1). In the SE region, Mn is detected with a confidence level greater than  $4\sigma$  (see Figure 1), whereas in the NW region Mn is not detected even at the  $1\sigma$  level. This makes it clear that the Mn abundance differs between these two areas. Moreover, when we compare the ratio of Mn to Cr, which is the element with the neighboring atomic number that should be synthesized in the same region, we find a Mn/Cr mass ratio of 0.65–0.68 in the SE region and Mn/Cr < 0.11 in the NW region (Table 1), showing a significant difference in their relative abundances. The result for the SW region lies between those for the SE and NW regions, suggesting that the Mn abundance varies from region to region in Cas A. In particular, as a neutron-rich odd-Z element, Mn serves as a tracer of the electron fraction and neutrino interactions in the nuclear-burning regions, making this asymmetric distribution especially intriguing (see section 4 for detail). The trend in the Mn abundance variation between the SE and NW regions remains consistent across different fitting conditions (Table 1), making it one of the most robust results of this study.

In addition to Mn, the abundance of another key neutron-rich element, Ni, also appears to vary among the regions. However, the uncertainties in plasma modeling for Ni remain large, and at present different atomic codes yield significantly different abundance estimates

(Plucinsky et al. 2025). This uncertainty arises primarily from the broad line profiles, which prevent clear separation of Fe  $\text{He}\beta$  emission from Ni  $\text{He}\alpha$  emission (see the zoom-up panel in Figure 3). In addition, differences between atomic codes in the emissivities of the various lines within this band further complicate these estimates. Determining the absolute Ni/Fe ratio is critical for inferring the physical conditions at the explosion center (see section 4), yet with the current data set an accurate estimate is challenging. We hope that future detailed non-equilibrium plasma modeling will help resolve these issues.

Although the detection significance is modest, the detection of Ti in the SE region at roughly the  $3\sigma$  level is noteworthy (see the zoom-up panel around the Ti  $\text{He}\alpha$  emission in Figure 3). The observed Ti/Fe ratio is 0.9–1.8, which agrees with the previous measurement with Chandra (see Sato et al. 2021, and section 4 for the detailed discussion). The energy scale for the Cas A observations was calibrated using on-board  $^{55}\text{Fe}$  sources, and the resulting systematic uncertainty in the reconstructed energy scale is <0.04 eV at 5.9 keV for the full detector array (see Methods in Xrism Collaboration et al. 2025, for more detail). In addition, the effect of thermal broadening near the Ti  $\text{He}\alpha$  emissions is  $\sim$ 20 eV, which is larger than the Resolve’s energy resolution of  $\sim$ 5 eV. Under the current conditions of energy-scale reconstruction and line broadening, the separation of the

**Table 1.** Best-fit parameters of spectral fits.

Region	SE		NW		SW		JET
Atomic Database	AtomDB	SPEX	AtomDB	SPEX	AtomDB	SPEX	AtomDB
Fitting parameters							
$(\text{Mg}/\text{H})/(\text{Mg}/\text{H})_{\odot}$	$3.8_{-0.2}^{+0.4}$	$5.3_{-0.6}^{+0.7}$	$1.8_{-0.2}^{+0.3}$	$3.6_{-0.5}^{+0.6}$	$1.3 \pm 0.3$	$3 \pm 1$	$6.5_{-0.6}^{+0.5}$
$(\text{Al}/\text{H})/(\text{Al}/\text{H})_{\odot}$	$5 \pm 1$	$3 \pm 1$	$3.4_{-0.7}^{+0.8}$	$3 \pm 1$	$<0.5$	$<2$	—
$(\text{Si}/\text{H})/(\text{Si}/\text{H})_{\odot}$	$7.5_{-0.3}^{+0.2}$	$7.5_{-0.3}^{+0.4}$	$4.32_{-0.06}^{+0.09}$	$5.3 \pm 0.2$	$1.91_{-0.09}^{+0.06}$	$2.3 \pm 0.2$	$8.0_{-0.4}^{+0.7}$
$(\text{P}/\text{H})/(\text{P}/\text{H})_{\odot}$	$10 \pm 1$	$6 \pm 1$	$4.7 \pm 0.8$	$3 \pm 1$	$4 \pm 1$	$5 \pm 2$	—
$(\text{S}/\text{H})/(\text{S}/\text{H})_{\odot}$	$7.8_{-0.1}^{+0.2}$	$7.2 \pm 0.3$	$5.20_{-0.08}^{+0.10}$	$5.8 \pm 0.2$	$2.31_{-0.09}^{+0.06}$	$2.5 \pm 0.2$	$8.0 \pm 0.6$
$(\text{Cl}/\text{H})/(\text{Cl}/\text{H})_{\odot}$	$11.8 \pm 0.9$	$7.4_{-0.9}^{+1.0}$	$7.4_{-0.6}^{+0.7}$	$6.1 \pm 0.8$	$3.2 \pm 0.7$	$3 \pm 2$	—
$(\text{Ar}/\text{H})/(\text{Ar}/\text{H})_{\odot}$	$7.0 \pm 0.2$	$6.0 \pm 0.3$	$4.81_{-0.06}^{+0.11}$	$5.3 \pm 0.1$	$2.36_{-0.09}^{+0.07}$	$2.6 \pm 0.2$	$7.5 \pm 0.6$
$(\text{K}/\text{H})/(\text{K}/\text{H})_{\odot}$	$9 \pm 1$	$8 \pm 1$	$5.3 \pm 0.7$	$6.1 \pm 0.9$	$1.8 \pm 0.8$	$2 \pm 2$	—
$(\text{Ca}/\text{H})/(\text{Ca}/\text{H})_{\odot}$	$7.0_{-0.2}^{+0.4}$	$6.3 \pm 0.3$	$5.27_{-0.07}^{+0.13}$	$5.8 \pm 0.2$	$2.75_{-0.12}^{+0.08}$	$3.0_{-0.2}^{+0.3}$	$9.0 \pm 0.8$
$(\text{Ti}/\text{H})/(\text{Ti}/\text{H})_{\odot}$	$4 \pm 2$	$6 \pm 2$	$<0.5$	$<0.3$	$3 \pm 2$	$<4$	$<1.7$
$(\text{Cr}/\text{H})/(\text{Cr}/\text{H})_{\odot}$	$5.0 \pm 0.6$	$4.9_{-0.6}^{+0.7}$	$3.1 \pm 0.5$	$3.2 \pm 0.6$	$3.0 \pm 0.7$	$3_{-1}^{+2}$	$<4.3$
$(\text{Mn}/\text{H})/(\text{Mn}/\text{H})_{\odot}$	$4 \pm 1$	$4 \pm 1$	$<0.3$	$<0.5$	$2 \pm 1$	$<6$	—
$(\text{Fe}/\text{H})/(\text{Fe}/\text{H})_{\odot}$	$11.4_{-0.4}^{+0.2}$	$7.9_{-0.5}^{+0.6}$	$6.64_{-0.05}^{+0.08}$	$6.2 \pm 0.3$	$3.5 \pm 0.2$	$3.0_{-0.3}^{+0.4}$	$3.0 \pm 0.4$
$(\text{Ni}/\text{H})/(\text{Ni}/\text{H})_{\odot}$	$15 \pm 1$	$5.3_{-0.6}^{+0.7}$	$7.5_{-0.8}^{+0.7}$	$3.5 \pm 0.6$	$6 \pm 1$	$3_{-1}^{+2}$	$7.1_{-2.6}^{+2.7}$
$kT_{e,1}$ [keV]	$0.89_{-0.02}^{+0.01}$	$0.75 \pm 0.2$	$0.69_{-0.01}^{+0.02}$	$0.58_{-0.02}^{+0.03}$	$0.87_{-0.06}^{+0.03}$	$0.82 \pm 0.06$	$1.1 \pm 0.1$
$kT_{e,2}$ [keV]	$2.41 \pm 0.02$	$2.90_{-0.08}^{+0.09}$	$2.54_{-0.03}^{+0.07}$	$2.37 \pm 0.05$	$2.34_{-0.07}^{+0.09}$	$2.3 \pm 0.2$	$3.1_{-0.3}^{+0.2}$
$n_{e1} [10^{10} \text{ cm}^{-3} \text{ s}]$	$4.9 \pm 0.3$	$32_{-3}^{+4}$	$4.1 \pm 0.3$	$5.2_{-0.5}^{+0.6}$	$60_{-10}^{+50}$	$>50$	$5.6_{-2.5}^{+4.9}$
$n_{e2} [10^{11} \text{ cm}^{-3} \text{ s}]$	$2.30_{-0.03}^{+0.05}$	$2.02 \pm 0.06$	$1.33_{-0.01}^{+0.02}$	$1.55 \pm 0.04$	$1.83 \pm 0.08$	$2.1_{-0.2}^{+0.3}$	$1.7_{-0.1}^{+0.2}$
Redshift $z_1 [10^{-3}]$	$-1.6 \pm 0.1$	$-1.6 \pm 0.1$	$0.07 \pm 0.01$	$6.09 \pm 0.07$	$0.51_{-0.08}^{+0.07}$	$0.5 \pm 0.1$	$4.3_{-0.9}^{+1.2}$
Redshift $z_2 [10^{-3}]$	$-4.15 \pm 0.04$	$-4.46 \pm 0.06$	$6.36 \pm 0.08$	$-0.1 \pm 0.3$	$4.2 \pm 0.1$	$4.2 \pm 0.3$	$-1.9 \pm 0.4$
RMS $V_1$ [km s $^{-1}$ ]	$1150 \pm 30$	$1230 \pm 30$	$1720 \pm 50$	$1730_{-60}^{+70}$	$490_{-30}^{+20}$	$500 \pm 50$	—
RMS $V_2$ [km s $^{-1}$ ]	$1290 \pm 10$	$1250 \pm 10$	$1830 \pm 10$	$1840 \pm 10$	$1850 \pm 40$	$1890 \pm 70$	—
$\frac{n_e n_p V_{\text{NEL},1}}{4\pi D^2} [10^{-14} \text{ cm}^{-5}]$	$0.70_{-0.02}^{+0.08}$	$1.4 \pm 0.1$	$1.88_{-0.05}^{+0.07}$	$2.6 \pm 0.3$	$1.6_{-0.1}^{+0.3}$	$2.0_{-0.4}^{+0.5}$	$0.5_{-0.1}^{+0.2}$
$\frac{n_e n_p V_{\text{NEL},2}}{4\pi D^2} [10^{-14} \text{ cm}^{-5}]$	$0.50 \pm 0.01$	$0.45 \pm 0.02$	$0.86 \pm 0.01$	$0.87 \pm 0.02$	$1.41_{-0.03}^{+0.04}$	$1.4 \pm 0.1$	$0.50 \pm 0.02$
Power-law index	2.3	2.3	2.3	2.3	2.3	2.3	2.3
Power-law norm	$0.055_{-0.005}^{+0.004}$	$0.022 \pm 0.007$	$0.077_{-0.001}^{+0.002}$	$0.088 \pm 0.003$	$0.26_{-0.02}^{+0.01}$	$0.26 \pm 0.03$	$0.07 \pm 0.02$
C-value/d.o.f	3652.63/3001	3748.35/3003	3847.30/3065	4165.77/3066	3214.40/2999	3316.26/3000	961.19/825
Mass ratios							
$M_{\text{Ca}}/M_{\text{Fe}} [10^{-2}]$	$3.2_{-0.1}^{+0.2}$	$4.1_{-0.3}^{+0.4}$	$4.0 \pm 0.1$	$4.8_{-0.2}^{+0.3}$	$4.0_{-0.3}^{+0.2}$	$5.1 \pm 0.1$	$15 \pm 2$
$M_{\text{Ti}}/M_{\text{Fe}} [10^{-3}]$	$0.9 \pm 0.4$	$1.8 \pm 0.6$	$<1.9$	$<1.4$	$2.2 \pm 1.4$	$<5.9$	$<1.4$
$M_{\text{Cr}}/M_{\text{Fe}} [10^{-3}]$	$4.8 \pm 0.8$	$6.8 \pm 1.3$	$5.1 \pm 1.1$	$5.8 \pm 1.4$	$9.6 \pm 3.0$	$10.8_{-6.3}^{+8.0}$	$<21$
$M_{\text{Mn}}/M_{\text{Cr}} [10^{-1}]$	$6.5 \pm 1.7$	$6.8 \pm 2.0$	$<0.8$	$<1.1$	$4.9 \pm 3.1$	$<15$	—
$M_{\text{Ni}}/M_{\text{Fe}} [10^{-2}]$	$8.1_{-0.7}^{+0.6}$	$4.1 \pm 0.6$	$6.7 \pm 0.7$	$6.8 \pm 2.0$	$11 \pm 2$	$5.5_{-2.4}^{+3.3}$	$14 \pm 6$

**Note.** The error shows  $1\sigma$  confidence level. The proto-solar abundances in Lodders et al. (2009) are used. The abundances are linked between the low-temperature (1) and high-temperature (2) components. For the analysis of the JET region with Xtend, the data were binned to ensure at least 20 counts per energy bin, and the spectra were fitted using  $\chi^2$  statistics. Even using the  $C$ -statistics, the values are consistent within the statistical error ranges. The unit of the power-law norm is [photons/keV/cm $^2$ /s] at 1 keV. Even when using a softer power-law index of 2.8 instead of the fixed power-law index (see Table 2), the conclusions of this study remain unchanged.

**Table 2.** Mass ratios with different fitting conditions.

Region ID.	$M_{\text{Ca}}/M_{\text{Fe}} [10^{-2}]$	$M_{\text{Ti}}/M_{\text{Fe}} [10^{-3}]$	$M_{\text{Cr}}/M_{\text{Fe}} [10^{-3}]$	$M_{\text{Mn}}/M_{\text{Cr}} [10^{-1}]$	$M_{\text{Ni}}/M_{\text{Fe}} [10^{-2}]$
Soft power-law index/AtomDB fit					
SE	$3.1^{+0.2}_{-0.4}$	$0.9 \pm 0.4$	$6.1^{+0.8}_{-1.1}$	$6.2^{+1.8}_{-1.7}$	$8.2^{+2.0}_{-1.3}$
NW	$4.1 \pm 0.1$	$< 0.2$	$6.8 \pm 1.2$	$< 1.0$	$6.5 \pm 0.7$
SW	$4.2 \pm 0.6$	$2.5^{+1.4}_{-1.5}$	$12 \pm 3$	$4.1 \pm 3.1$	$10 \pm 4$
Soft power-law index/SPEX fit					
SE	$4.1 \pm 0.7$	$1.8 \pm 0.6$	$8.9^{+2.3}_{-2.2}$	$6.9^{+2.7}_{-2.5}$	$4.1^{+1.1}_{-1.0}$
NW	$5.0 \pm 0.4$	$< 0.2$	$8.4 \pm 1.4$	$< 1.4$	$3.0 \pm 0.6$
SW	$5.3 \pm 0.9$	$2.3^{+2.0}_{-2.1}$	$14^{+4}_{-5}$	$5.3^{+4.8}_{-4.6}$	$5.2 \pm 1.9$
$N_{\text{H}}$ free/AtomDB fit					
SE	$3.0 \pm 0.3$	$1.1 \pm 0.5$	$6.5^{+0.6}_{-0.8}$	$6.7 \pm 1.7$	$7.9^{+0.7}_{-1.0}$
NW	$4.5 \pm 0.2$	$< 0.5$	$8.1^{+1.4}_{-1.3}$	$< 1.2$	$4.6 \pm 0.6$
SW	$4.1 \pm 0.3$	$2.4 \pm 1.6$	$12 \pm 4$	$4.5^{+3.2}_{-3.1}$	$10 \pm 2$

**Note.** The error shows  $1\sigma$  confidence level. In the “soft power-law index” fit, the power-law index was fixed at 2.8.

Ti He $\alpha$  line from the neighboring Ca He $\beta/\gamma$  line complex on either side is achievable, enabling a more precise measurement than was possible with the previous Chandra observations. In the NW and SW regions, Ti is not detected at a statistically significant level (at  $< 1\sigma$  level). One reason may be that, compared to the SE region, these regions have a larger contribution from non-thermal emission, resulting in a lower signal-to-noise ratio. In these regions, we also found that the detection significance or upper limit for Ti changes depending on variations in the parameters of the interstellar absorption and the power-law component (Table 2). In the future, deeper observations will be necessary to determine the Ti abundance in those regions.

In some fittings, the temperature and ionization age of the low-temperature component differ between AtomDB and SPEX. This is likely due to the difficulty of fitting caused by the lack of emission below 1 keV. On the other hand, the emissions from the Fe-group elements mainly depends on the high-temperature component, and we have confirmed that the uncertainties in the low-temperature component’s parameters do not affect our conclusions.

We also investigated the presence of Fe-peak elements in the northeastern jet structure using XRISM/Xtend. As in the other regions, the spectral fitting was performed with a model consisting of a two-temperature plasma component plus an additional power-law. For the abundances of odd-Z elements and the line broadening, which are difficult to constrain with Xtend, the parameters were fixed to the values obtained in the SE region with Resolve. Although weak emission lines such as Ti, Cr, and Mn were not significantly detected, the low background level enabled us to identify a prominent emission-line structure around the Ni band. Consequently, the analysis yields a relatively large mass ratio

of Ni/Fe =  $0.14 \pm 0.6$ . While systematic uncertainties among atomic codes remain substantial for Ni, this result may suggest a contribution from the  $\alpha$ -rich freeze-out region near the explosion center (see also Sapienza et al. 2025). A more detailed analysis based on Xtend will be presented in a forthcoming paper (Kurashima et al., in preparation).

#### 4. COMPARISON WITH THEORETICAL CALCULATIONS

In this study, we for the first time demonstrated that the Fe-peak elemental composition within Cas A differs among the three Fe-rich blobs using the high-energy resolution observations with XRISM/Resolve. In particular, the SE region exhibits high Mn/Cr and Ni/Fe ratios, whereas those ratios are significantly lower in the NW region, suggesting that explosion asymmetries may have generated these abundance differences. In this section, we compare our findings with a multidimensional supernova simulation to discuss which physical processes produce the asymmetric distribution of Fe-peak elements in Cas A.

Figure 4 compares the elemental mass ratios derived from each region we observed with those in individual fluid elements of a two-dimensional SN model. This model is based on the explosion calculations of Fujimoto et al. (2011) for a  $21 M_{\odot}$  progenitor calculated by Rauscher et al. (2002), with an explosion energy of  $\approx 10^{51}$  erg (see also Fujimoto & Nagakura 2021). The simulation implements a neutrino-driven mechanism aided by standing accretion shock instability (SASI) and convection, thereby incorporating the asymmetric effects expected in core-collapse SNe. The calculation was carried out up to  $\sim 1$  s after the explosion, and only those fluid elements that escape the gravitational potential of the proto-neutron star are included in the comparison.

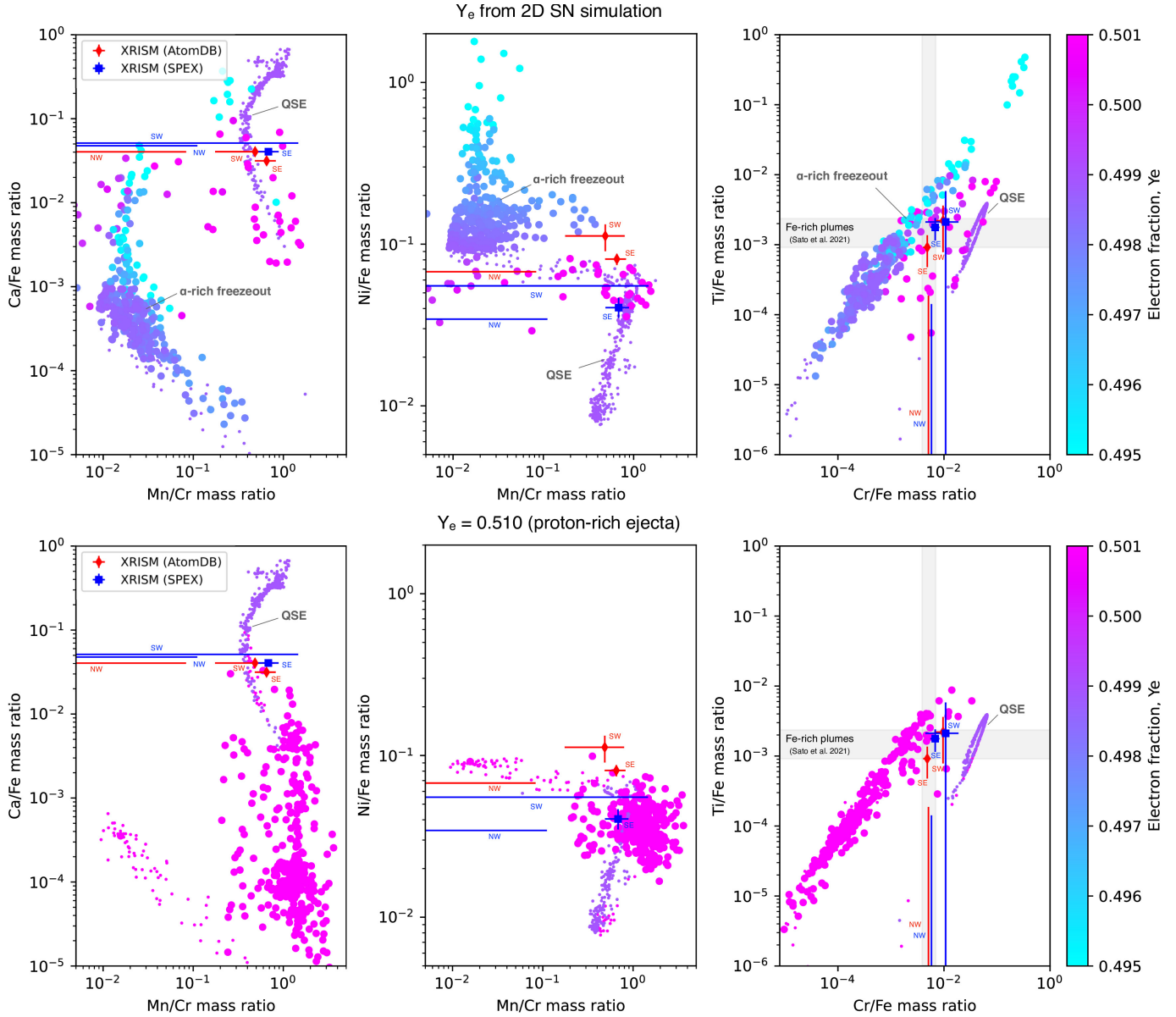


**Figure 4.** *Top panels:* Comparison of the elemental mass ratios in individual fluid elements of a 2D supernova model with those observed in Cas A. From left to right, the Mn/Cr versus Ca/Fe plot, the Mn/Cr versus Ni/Fe plot, and the Cr/Fe versus Ti/Fe plot are shown. Model points are colored by their electron fraction ( $Y_e$ ), with light blue indicating low  $Y_e$  regions and magenta indicating high  $Y_e$  regions. Data points for  $T_{\text{peak}} > 5.5$  GK (i.e., complete Si burning or  $\alpha$ -rich freezeout) are represented by large circles, whereas those for  $T_{\text{peak}} < 5.5$  GK (i.e., incomplete Si burning or quasi-equilibrium: QSE) are represented by small circles. Observational values appear as red and blue data points with error bars ( $1\sigma$  confidence level). In the Ti/Fe vs. Cr/Fe plot, the observational values reported in Sato et al. (2021) are indicated by gray areas. *Bottom panels:* Same as the top panels, but compared with nucleosynthesis calculations with the electron fraction fixed at  $Y_e = 0.51$ , resembling a case where most of the ejecta become proton-rich ( $Y_e > 0.5$ ) owing to neutrino irradiation. The electron fraction is fixed only for ejecta with peak temperatures exceeding 5.5 GK. The observational values in these plots are taken from Table 1.

Neutrino reactions are also included in the nucleosynthesis calculations, allowing their influence to be compared directly with the observational results. In deriving the elemental mass ratios, the calculations are carried out in the stable state after all decay processes of unstable isotopes have been completed. For the comparison, we use the inner ejecta by selecting zones with an O/Fe mass ratio below 0.1. The small marker points in Figure 4 represent the ejecta from the incomplete Si burning (i.e., quasi-equilibrium: QSE) and thus the large marker points reflect the composition of the complete Si burning region. The color of each model data point in the figure indicates the electron fraction, illustrating the transition from neutron-rich ejecta (light blue) to proton-rich ejecta (pink).

Figure 4 top left shows a comparison of the Ca/Fe and Mn/Cr ratios with theoretical predictions. Because Ca is produced primarily in the incomplete Si-burning region (e.g., Thielemann & Arnett 1985; Woosley & Weaver 1995), its abundance serves as an indicator of the degree of contamination from that region. In particular, for XISM/Resolve observations, the telescope’s point spread function and the  $0.5' \times 0.5'$  size of the Resolve pixels (Tashiro et al. 2025) make it difficult to isolate regions purely rich in Fe, and explosion-driven mixing is expected to blend compositions from multiple burning layers.

The most observationally significant and interesting result is that the Mn abundance differs among the regions. In our current comparison, the Mn/Cr ratio in the SE region aligns with those in the incomplete Si-burning zone, whereas in the NW region it appears to match the ratios in the  $\alpha$ -rich freezeout (complete Si-burning) zone. This is exactly opposite to the trend indicated by the Ca/Fe ratio, where the higher Ca abundance in the NW region implies greater contamination from the incomplete Si-burning zone. Therefore, these observational results cannot be explained by mixing effects alone. If the Mn/Cr ratio reflects the nucleosynthesis in the  $\alpha$ -rich freezeout region, then this variation in Mn abundance may signal differences in the extent of neutrino processing. Sato et al. (2023) have also detected Mn in the Fe-rich structure in Cas A’s southeast region and demonstrated that neutrino emission of  $(3\text{--}5)\times 10^{53}$  erg from a SN assuming a typical neutron star mass can account for its synthesis (see also Yoshida et al. 2008). In the theoretical models we compared, the neutrino luminosity is of order of  $10^{52}$  erg, but if in reality it were an order of magnitude higher and spatially dependent, it might explain the asymmetric Mn/Cr distribution observed in Cas A. However, once mixing and overlap from other regions are taken into account, the

current data set does not allow us to conclusively identify the underlying cause.

Figure 4 top middle shows the distribution of another important neutron-rich element, Ni. In the case of Ni, different atomic codes (AtomDB and SPEX) currently yield different absolute abundances (see Plucinsky et al. 2025, for detail), making a discussion of its absolute value difficult. However, the trend that the Ni/Fe ratio is lowest in the NW region and highest in the SW region is consistent across both atomic codes. For example, the AtomDB-based evaluation finds a Ni/Fe mass ratio of  $\sim 0.07\text{--}0.1$ , whereas SPEX shows values in the range of  $\sim 0.03\text{--}0.06$ . Since almost all Ni is synthesized in the complete Si-burning region (e.g., Thielemann & Arnett 1985; Woosley & Weaver 1995), this variation in Ni/Fe likely reflects differences in the physical conditions near the explosion center. In particular, the electron fraction,  $Y_e$  (i.e., neutron excess), is an important parameter for determining Ni/Fe, and  $Y_e$  is expected to vary within the SN interior due to two main factors: (a) differences in local neutrino irradiation and (b) variations in the progenitor’s internal  $Y_e$ .

Regarding the scenario (a), the  $21 M_\odot$  model we compared already incorporates these effects, its theoretical predictions span a wide range of  $M_{\text{Ni}}/M_{\text{Fe}} \sim 0.03\text{--}1.0$ . For example, materials subjected to intense neutrino irradiation undergo charge-current interactions (i.e.,  $n + \nu_e \rightarrow p + e^-$ ), becoming proton-rich (high  $Y_e$  of  $> 0.5$ ) (e.g., Fröhlich et al. 2006b,a; Janka 2012; Wanajo et al. 2018; Vartanyan et al. 2018; Burrows et al. 2024), whereas materials in the innermost regions that have escaped from neutrinos could remain neutron-rich (low  $Y_e$  of  $< 0.5$ ) in our calculations. The values derived from AtomDB are located at around the model’s peak region, while those from SPEX concentrate toward the lower end of this range. Observational values showing Ni/Fe mass ratios below 0.07 are found in both SPEX and AtomDB analyses, suggesting ejecta with  $Y_e \approx 0.5$  or higher. Explaining these observations may require either low initial metallicity of the progenitor as proposed in Sato et al. (2020) or proton-rich ejecta that have been heavily processed by neutrinos (Sato et al. 2021). Interestingly, the observed values (especially those in the SE region) seem to agree well with the proton-rich ejecta predicted by the model. This may suggest that a large fraction of the innermost ejecta has been exposed to neutrinos strongly enough to become proton-rich. The bottom panels of Figure 4 show a comparison with nucleosynthesis calculations in which the electron fractions were fixed at  $Y_e = 0.51$ , resembling a state where most of the ejecta become proton-rich as a result of neutrino irradiation. Interestingly, the mass ratios of Mn/Cr,

Ni/Fe, Ti/Fe, and Cr/Fe are in good agreement with these proton-rich cases (see also Sato et al. 2021). Recent multi-dimensional simulations have further demonstrated that, especially in the case of massive progenitors, ejecta with  $Y_e \geq 0.5$  can dominate (e.g., Wang & Burrows 2024), making the similarity to Cas A particularly noteworthy.

Regarding the scenario (b), multidimensional simulations of a massive star in the final evolutionary stages predict that intense oxygen burning drives significant mixing beyond convective boundaries and alters the internal distribution of the electron fraction,  $Y_e$  (e.g., Bazan & Arnett 1994). This phenomenon, known as “shell merger”, has been reproduced in various theoretical calculations (e.g., Arnett & Meakin 2011; Yoshida et al. 2019; Yadav et al. 2020; Yoshida et al. 2021; Rizzuti et al. 2024), and it has been suggested that Cas A’s progenitor also experienced such an inhomogeneous shell-merger mixing just before the SN explosion (Sato et al. 2025b,c). Therefore, it would be plausible that this stellar mixing generated an asymmetric  $Y_e$  distribution in the progenitor, giving rise to the asymmetric Ni/Fe and Mn/Cr ratios. Furthermore, this effect may have enhanced the explosion asymmetry of the supernova (e.g., Müller et al. 2017; Bollig et al. 2021).

The stable Ti we observed will also provide important insights into discussions of asymmetric explosions (Figure 4 right). As with the well-known radioactive isotope  $^{44}\text{Ti}$  (e.g., Grefenstette et al. 2014; Boggs et al. 2015), stable Ti (predominantly  $^{48}\text{Ti}$ ) is synthesized in amounts that vary with the entropy at the explosion center, making it a valuable tracer of asymmetric explosions (e.g., Sato et al. 2021, 2025a). Recently, Sato et al. (2021) reported the detection of stable Ti in the southeast Fe-rich region and argued that this structure represents high-entropy plumes produced by neutrino heating during the explosion. Despite the much lower photon statistics compared to previous Chandra observations, we leveraged XRISM/Resolve’s superior energy resolution to reassess these synthesized abundances and obtained results that agree with the previous findings (see the SE values in Figure 4 right). Although we did not achieve significant detections in the NW and SW regions at present, future deeper observations should enable us to discuss the distribution of Ti as well.

We note that the model employed in this work is a 2D (axisymmetric) simulation that was evolved up to  $\sim 1$  s after core bounce. In such 2D models, hydrodynamic instabilities such as neutrino-driven convection and SASI are artificially constrained by axial symmetry, producing coherent, axis-aligned plumes that differ from the more stochastic, multi-directional structures found in

3D simulations (e.g., Hanke et al. 2012; Takiwaki et al. 2014; Müller 2016). Moreover, since the model represents an early post-bounce phase, it does not include the later evolution involving the Ni-bubble effect (e.g., Wongwathanarat et al. 2015), reverse shocks, and chemical mixing over hundreds of years (e.g., Orlando et al. 2016, 2021). Therefore, our comparison with this model should be regarded as qualitative, aiming to illustrate possible trends in  $Y_e$ -dependent nucleosynthesis rather than a one-to-one match to present-day ejecta morphology. We also note that recent three-dimensional simulations that follow the evolution from pre-collapse convection through core collapse and explosion (e.g., Müller et al. 2017; Bollig et al. 2021; Vartanyan et al. 2025) generally predict less coherent and more stochastic mixing, along with highly complex distributions of Fe-peak elements. In these models, multi-dimensional perturbations present in the Si/O shells before collapse are amplified during the explosion and lead to strongly asymmetric, small-scale structures in the Fe-rich ejecta, in stark contrast to the artificially coherent, axis-aligned plumes produced in 2D simulations.

## 5. SUMMARY AND CONCLUSION

In this work, we have employed high-resolution X-ray spectroscopy with XRISM/Resolve to perform a detailed compositional analysis of Fe-peak elements (Ti, Cr, Mn, Ni, Fe) in three distinct Fe-rich regions (SE, NW, SW) of Cas A. Our observations reveal a significant detection ( $> 4\sigma$ ) of Mn He $\alpha$  emission in the SE region, with negligible Mn in the NW, alongside pronounced regional variations in Mn/Cr, Ni/Fe, and Ti/Fe ratios. It would be difficult to explain such asymmetries based solely on simple matter mixing and instead point to a combination of effects: (1) differential mixing of material from various Si-burning layers at the time of explosion, (2) spatial inhomogeneities in the electron fraction ( $Y_e$ ) within the progenitor and near the explosion center, and (3) locally dependent enhancements of  $\nu$ -process and  $\nu p$ -process nucleosynthesis driven by neutrino irradiation. These results provide new insights from a different perspective into previous studies of the asymmetry in Cas A (e.g., Grefenstette et al. 2014; Milisavljevic & Fesen 2015; Sato et al. 2021), suggesting that the asymmetric structures may have possessed different physical conditions during the explosion.

Comparison with multidimensional, neutrino-driven explosion models indicates that the observed abundance asymmetries could be linked to variations in the electron fraction ( $Y_e$ ) and/or neutrino irradiation in the innermost ejecta. The high Mn/Cr ratio in the SE region is consistent with proton-rich conditions ( $Y_e > 0.5$ )

produced by intense neutrino processing, whereas the suppressed Mn/Cr ratio in the NW region suggests  $\alpha$ -rich freeze-out. The observed diversity in Ni/Fe ratios also supports local  $Y_e$  variations, either originating from asymmetric neutrino irradiation or from asymmetric mixing in the progenitor's late evolutionary stages. In addition, the marginal detection of stable Ti in the SE region may support the high-entropy ejecta driven by neutrino heating as previously reported. These results highlight that both neutrino interactions and progenitor mixing processes likely played critical roles in producing the asymmetric distribution of Fe-peak elements in Cas A.

Our findings offer crucial constraints on the asymmetric mechanisms at play in core-collapse supernovae and on the role of neutrino irradiation in shaping the earliest phases of element synthesis. Future efforts, combining finer spatial-resolution spectroscopy with XRISM's expanded mapping capabilities, next-generation microcalorimeter missions (e.g., Kraft et al. 2024), and three-dimensional explosion simulations (e.g., Orlando et al. 2024), will be essential for quantitatively disentangling the physical processes driving asymmetry in supernova explosions.

tangling the physical processes driving asymmetry in supernova explosions.

**Acknowledgments:** We thank all of the scientists, engineers, and technicians that built the XRISM satellite, operate the mission, and developed the software that we used to analyze the data in this paper. We also thank the anonymous referee for their careful reading of the manuscript and for constructive comments and suggestions that significantly improved the clarity and quality of this paper. This work was partly supported by Japan Society for the Promotion of Science Grants-in-Aid for Scientific Research (KAKENHI) Grant Numbers, JP23K25907 (AB), JP23K13128 (TS). This work was supported by the JSPS Core-to-Core Program (grant number: JPJSCCA20220002) (YT) and the Japan Society for the Promotion of Science Grants-in-Aid for Scientific Research (KAKENHI) Grant Number JP20K04009 (YT). PP acknowledges support from NASA XRISM grants 80NSSC18K0988 and 80NSSC23K1656, and the Smithsonian Institution and the Chandra X-ray Center through NASA contract NAS8-03060. MA and JV acknowledge financial support from NWO under grant number 184.034.002. This work was supported by the Mitsubishi Foundation.

## REFERENCES

Arnaud, K. A. 1996, in Astronomical Society of the Pacific Conference Series, Vol. 101, Astronomical Data Analysis Software and Systems V, ed. G. H. Jacoby & J. Barnes, 17

Arnett, W. D., & Meakin, C. 2011, The Astrophysical Journal, 733, 78, doi: [10.1088/0004-637X/733/2/78](https://doi.org/10.1088/0004-637X/733/2/78)

Badenes, C., Bravo, E., & Hughes, J. P. 2008, ApJL, 680, L33, doi: [10.1086/589832](https://doi.org/10.1086/589832)

Bamba, A., Agarwal, M., Vink, J., et al. 2025, PASJ, doi: [10.1093/pasj/psaf041](https://doi.org/10.1093/pasj/psaf041)

Bazan, G., & Arnett, D. 1994, ApJL, 433, L41, doi: [10.1086/187543](https://doi.org/10.1086/187543)

Boggs, S. E., Harrison, F. A., Miyasaka, H., et al. 2015, Science, 348, 670, doi: [10.1126/science.aaa2259](https://doi.org/10.1126/science.aaa2259)

Bollig, R., Yadav, N., Kresse, D., et al. 2021, The Astrophysical Journal, 915, 28, doi: [10.3847/1538-4357/abf82e](https://doi.org/10.3847/1538-4357/abf82e)

Burrows, A., & Vartanyan, D. 2021, Nature, 589, 29, doi: [10.1038/s41586-020-03059-w](https://doi.org/10.1038/s41586-020-03059-w)

Burrows, A., Wang, T., & Vartanyan, D. 2024, ApJL, 964, L16, doi: [10.3847/2041-8213/ad319e](https://doi.org/10.3847/2041-8213/ad319e)

Cash, W. 1979, Astrophysical Journal, Part 1, vol. 228, Mar. 15, 1979, p. 939-947., 228, 939

Fesen, R. A., Hammell, M. C., Morse, J., et al. 2006, ApJ, 636, 859, doi: [10.1086/498092](https://doi.org/10.1086/498092)

Fröhlich, C., Martínez-Pinedo, G., Liebendörfer, M., et al. 2006a, PhRvL, 96, 142502, doi: [10.1103/PhysRevLett.96.142502](https://doi.org/10.1103/PhysRevLett.96.142502)

Fröhlich, C., Hauser, P., Liebendörfer, M., et al. 2006b, ApJ, 637, 415, doi: [10.1086/498224](https://doi.org/10.1086/498224)

Fujimoto, S.-i., Kotake, K., Hashimoto, M.-a., Ono, M., & Ohnishi, N. 2011, ApJ, 738, 61, doi: [10.1088/0004-637X/738/1/61](https://doi.org/10.1088/0004-637X/738/1/61)

Fujimoto, S.-i., & Nagakura, H. 2021, MNRAS, 502, 2319, doi: [10.1093/mnras/stab171](https://doi.org/10.1093/mnras/stab171)

Grefenstette, B. W., Harrison, F. A., Boggs, S. E., et al. 2014, Nature, 506, 339, doi: [10.1038/nature12997](https://doi.org/10.1038/nature12997)

Hanke, F., Marek, A., Müller, B., & Janka, H.-T. 2012, ApJ, 755, 138, doi: [10.1088/0004-637X/755/2/138](https://doi.org/10.1088/0004-637X/755/2/138)

Hayakawa, T., Nakamura, K., Kajino, T., et al. 2013, ApJL, 779, L9, doi: [10.1088/2041-8205/779/1/L9](https://doi.org/10.1088/2041-8205/779/1/L9)

Hayakawa, T., Ko, H., Cheoun, M.-K., et al. 2018, PhRvL, 121, 102701, doi: [10.1103/PhysRevLett.121.102701](https://doi.org/10.1103/PhysRevLett.121.102701)

Heger, A., Kolbe, E., Haxton, W. C., et al. 2005, Physics Letters B, 606, 258, doi: [10.1016/j.physletb.2004.12.017](https://doi.org/10.1016/j.physletb.2004.12.017)

Hughes, J. P., Rakowski, C. E., Burrows, D. N., & Slane, P. O. 2000, *ApJL*, 528, L109, doi: [10.1086/312438](https://doi.org/10.1086/312438)

Hwang, U., & Laming, J. M. 2012, *ApJ*, 746, 130, doi: [10.1088/0004-637X/746/2/130](https://doi.org/10.1088/0004-637X/746/2/130)

Ishisaki, Y., Kelley, R. L., Awaki, H., et al. 2025, *Journal of Astronomical Telescopes, Instruments, and Systems*, 11, 042023, doi: [10.1117/1.JATIS.11.4.042023](https://doi.org/10.1117/1.JATIS.11.4.042023)

Janka, H.-T. 2012, *Annual Review of Nuclear and Particle Science*, 62, 407, doi: [10.1146/annurev-nucl-102711-094901](https://doi.org/10.1146/annurev-nucl-102711-094901)

Jerkstrand, A., Timmes, F. X., Magkotsios, G., et al. 2015, *ApJ*, 807, 110, doi: [10.1088/0004-637X/807/1/110](https://doi.org/10.1088/0004-637X/807/1/110)

Kaastra, J. S., Mewe, R., & Nieuwenhuijzen, H. 1996, in *UV and X-ray Spectroscopy of Astrophysical and Laboratory Plasmas*, 411–414

Kraft, R., Bogdán, Á., ZuHone, J., et al. 2024, in *Society of Photo-Optical Instrumentation Engineers (SPIE) Conference Series*, Vol. 13093, *Space Telescopes and Instrumentation 2024: Ultraviolet to Gamma Ray*, ed. J.-W. A. den Herder, S. Nikzad, & K. Nakazawa, 1309327, doi: [10.1117/12.3019969](https://doi.org/10.1117/12.3019969)

Lodders, K., Palme, H., & Gail, H. P. 2009, *Landolt Börnstein*, 4B, 712, doi: [10.1007/978-3-540-88055-4\\_34](https://doi.org/10.1007/978-3-540-88055-4_34)

Milisavljevic, D., & Fesen, R. A. 2015, *Science*, 347, 526, doi: [10.1126/science.1261949](https://doi.org/10.1126/science.1261949)

Milisavljevic, D., Temim, T., De Looze, I., et al. 2024, *ApJL*, 965, L27, doi: [10.3847/2041-8213/ad324b](https://doi.org/10.3847/2041-8213/ad324b)

Mori, K., Tomida, H., Nakajima, H., et al. 2024, in *Society of Photo-Optical Instrumentation Engineers (SPIE) Conference Series*, Vol. 13093, *Space Telescopes and Instrumentation 2024: Ultraviolet to Gamma Ray*, ed. J.-W. A. den Herder, S. Nikzad, & K. Nakazawa, 130931I, doi: [10.1117/12.3019804](https://doi.org/10.1117/12.3019804)

Müller, B. 2016, *PASA*, 33, e048, doi: [10.1017/pasa.2016.40](https://doi.org/10.1017/pasa.2016.40)

Müller, B., Melson, T., Heger, A., & Janka, H.-T. 2017, *Monthly Notices of the Royal Astronomical Society*, 472, 491, doi: [10.1093/mnras/stx1962](https://doi.org/10.1093/mnras/stx1962)

Orlando, S., Miceli, M., Pumo, M. L., & Bocchino, F. 2016, *ApJ*, 822, 22, doi: [10.3847/0004-637X/822/1/22](https://doi.org/10.3847/0004-637X/822/1/22)

Orlando, S., Wongwathanarat, A., Janka, H. T., et al. 2021, *A&A*, 645, A66, doi: [10.1051/0004-6361/202039335](https://doi.org/10.1051/0004-6361/202039335)

Orlando, S., Miceli, M., Patnaude, D. J., et al. 2024, *arXiv e-prints*, arXiv:2408.12462, doi: [10.48550/arXiv.2408.12462](https://doi.org/10.48550/arXiv.2408.12462)

Orlando, S., Janka, H. T., Wongwathanarat, A., et al. 2025, *A&A*, 696, A108, doi: [10.1051/0004-6361/202553833](https://doi.org/10.1051/0004-6361/202553833)

Park, S., Badenes, C., Mori, K., et al. 2013, *ApJL*, 767, L10, doi: [10.1088/2041-8205/767/1/L10](https://doi.org/10.1088/2041-8205/767/1/L10)

Plucinsky, P., Agarwal, M., Gu, L., et al. 2025, *PASJ*, 77, S171, doi: [10.1093/pasj/psaf091](https://doi.org/10.1093/pasj/psaf091)

Rauscher, T., Heger, A., Hoffman, R. D., & Woosley, S. E. 2002, *ApJ*, 576, 323, doi: [10.1086/341728](https://doi.org/10.1086/341728)

Rizzuti, F., Hirschi, R., Varma, V., et al. 2024, *Monthly Notices of the Royal Astronomical Society*, 533, 687, doi: [10.1093/mnras/stae1778](https://doi.org/10.1093/mnras/stae1778)

Sapienza, V., Miceli, M., Ono, M., et al. 2025, *ApJL*, 990, L5, doi: [10.3847/2041-8213/adf6bd](https://doi.org/10.3847/2041-8213/adf6bd)

Sato, T., Sawada, M., Maeda, K., Hughes, J. P., & Williams, B. J. 2025a, *ApJ*, 986, 94, doi: [10.3847/1538-4357/add932](https://doi.org/10.3847/1538-4357/add932)

Sato, T., Yoshida, T., Umeda, H., et al. 2023, *ApJ*, 954, 112, doi: [10.3847/1538-4357/ace7c1](https://doi.org/10.3847/1538-4357/ace7c1)

—. 2020, *ApJ*, 893, 49, doi: [10.3847/1538-4357/ab822a](https://doi.org/10.3847/1538-4357/ab822a)

Sato, T., Maeda, K., Nagataki, S., et al. 2021, *Nature*, 592, 537, doi: [10.1038/s41586-021-03391-9](https://doi.org/10.1038/s41586-021-03391-9)

Sato, T., Matsunaga, K., Sawada, R., et al. 2025b, *ApJ*, 984, 185, doi: [10.3847/1538-4357/adc68d](https://doi.org/10.3847/1538-4357/adc68d)

Sato, T., Matsunaga, K., Uchida, H., et al. 2025c, *ApJ*, 990, 103, doi: [10.3847/1538-4357/aded14](https://doi.org/10.3847/1538-4357/aded14)

Sieverding, A., Langanke, K., Martínez-Pinedo, G., et al. 2019, *ApJ*, 876, 151, doi: [10.3847/1538-4357/ab17e2](https://doi.org/10.3847/1538-4357/ab17e2)

Sieverding, A., Martínez-Pinedo, G., Huther, L., Langanke, K., & Heger, A. 2018, *ApJ*, 865, 143, doi: [10.3847/1538-4357/aadd48](https://doi.org/10.3847/1538-4357/aadd48)

Suzuki, S., Sonoda, H., Sakai, Y., et al. 2025, *PASJ*, doi: [10.1093/pasj/psaf040](https://doi.org/10.1093/pasj/psaf040)

Takiwaki, T., Kotake, K., & Suwa, Y. 2014, *ApJ*, 786, 83, doi: [10.1088/0004-637X/786/2/83](https://doi.org/10.1088/0004-637X/786/2/83)

Tashiro, M., Kelley, R., Watanabe, S., et al. 2025, *PASJ*, doi: [10.1093/pasj/psaf023](https://doi.org/10.1093/pasj/psaf023)

Thielemann, F. K., & Arnett, W. D. 1985, *ApJ*, 295, 604, doi: [10.1086/163403](https://doi.org/10.1086/163403)

Thielemann, F.-K., Nomoto, K., & Hashimoto, M.-A. 1996, *ApJ*, 460, 408, doi: [10.1086/176980](https://doi.org/10.1086/176980)

Timmes, F. X., Brown, E. F., & Truran, J. W. 2003, *ApJL*, 590, L83, doi: [10.1086/376721](https://doi.org/10.1086/376721)

Vartanyan, D., Burrows, A., Radice, D., Skinner, M. A., & Dolence, J. 2018, *MNRAS*, 477, 3091, doi: [10.1093/mnras/sty809](https://doi.org/10.1093/mnras/sty809)

Vartanyan, D., Tsang, B. T.-H., Kasen, D., et al. 2025, *ApJ*, 982, 9, doi: [10.3847/1538-4357/adb1e4](https://doi.org/10.3847/1538-4357/adb1e4)

Vink, J., Agarwal, M., Bamba, A., et al. 2025, *PASJ*, 77, psaf053, doi: [10.1093/pasj/psaf053](https://doi.org/10.1093/pasj/psaf053)

Wanajo, S., Müller, B., Janka, H.-T., & Heger, A. 2018, *ApJ*, 852, 40, doi: [10.3847/1538-4357/aa9d97](https://doi.org/10.3847/1538-4357/aa9d97)

Wang, T., & Burrows, A. 2024, *ApJ*, 962, 71, doi: [10.3847/1538-4357/ad12b8](https://doi.org/10.3847/1538-4357/ad12b8)

Wongwathanarat, A., Janka, H.-T., Müller, E., Pllumbi, E., & Wanajo, S. 2017, *ApJ*, 842, 13, doi: [10.3847/1538-4357/aa72de](https://doi.org/10.3847/1538-4357/aa72de)

Wongwathanarat, A., Müller, E., & Janka, H. T. 2015, *A&A*, 577, A48, doi: [10.1051/0004-6361/201425025](https://doi.org/10.1051/0004-6361/201425025)

Woosley, S. E., Arnett, W. D., & Clayton, D. D. 1973, *ApJS*, 26, 231, doi: [10.1086/190282](https://doi.org/10.1086/190282)

Woosley, S. E., Hartmann, D. H., Hoffman, R. D., & Haxton, W. C. 1990, *ApJ*, 356, 272, doi: [10.1086/168839](https://doi.org/10.1086/168839)

Woosley, S. E., & Haxton, W. C. 1988, *Nature*, 334, 45, doi: [10.1038/334045a0](https://doi.org/10.1038/334045a0)

Woosley, S. E., & Weaver, T. A. 1995, *ApJS*, 101, 181, doi: [10.1086/192237](https://doi.org/10.1086/192237)

Xrism Collaboration, Marc, A., Awaki, H., Ballhausen, R., et al. 2025, *Nature Astronomy*, doi: [10.1038/s41550-025-02714-4](https://doi.org/10.1038/s41550-025-02714-4)

Yadav, N., Müller, B., Janka, H. T., Melson, T., & Heger, A. 2020, *The Astrophysical Journal*, 890, 94, doi: [10.3847/1538-4357/ab66bb](https://doi.org/10.3847/1538-4357/ab66bb)

Yoshida, T., Kajino, T., & Hartmann, D. H. 2005, *PhRvL*, 94, 231101, doi: [10.1103/PhysRevLett.94.231101](https://doi.org/10.1103/PhysRevLett.94.231101)

Yoshida, T., Takiwaki, T., Aguilera-Dena, D. R., et al. 2021, *Monthly Notices of the Royal Astronomical Society*, 506, L20, doi: [10.1093/mnrasl/slab067](https://doi.org/10.1093/mnrasl/slab067)

Yoshida, T., Takiwaki, T., Kotake, K., et al. 2019, *ApJ*, 881, 16, doi: [10.3847/1538-4357/ab2b9d](https://doi.org/10.3847/1538-4357/ab2b9d)

Yoshida, T., Umeda, H., & Nomoto, K. 2008, *ApJ*, 672, 1043, doi: [10.1086/523833](https://doi.org/10.1086/523833)